

Effect of Reaction Layers on Internal Stresses in Co-Fired Multilayers of Calcium Manganate and Calcium Cobaltite

Patrick Stargardt, Sophie Bresch, Rainer Falkenberg, and Björn Mieller*

A widespread recovery of waste heat requires a cost-effective production of thermoelectric generators. Thermoelectric oxides are predestined for use at high temperatures. For manufacturing reasons, a multilayer generator design will be easily scalable and cost-effective. To evaluate the potential of ceramic multilayer technology for that purpose, a multilayer of the promising thermoelectric oxides calcium cobaltite ($\text{Ca}_3\text{Co}_4\text{O}_9$), calcium manganate (CMO, CaMnO_3), and glass-ceramic insulation layers is fabricated. Cracks and reaction layers at the interfaces are observed in the microstructure. The compositions of these reaction layers are identified by energy-dispersive X-ray spectroscopy and X-ray diffraction. Mechanical and thermal properties of all layers are compiled from literature or determined by purposeful sample preparation and testing. Based on this data set, the internal stresses in the multilayer after co-firing are calculated numerically. It is shown that tensile stresses in the range of 50 MPa occur in the CMO layers. The reaction layers have only a minor influence on the level of these residual stresses. Herein, it is proven that the material system is basically suitable for multilayer generator production, but that the co-firing process and the layer structure must be adapted to improve densification and reduce the tensile stresses in the CMO.

1. Introduction

The conversion of waste heat into electrical power by exploiting the thermoelectric effect is gaining increasing attention for a wide variety of applications.^[1] Thermoelectric oxides are particularly suited for high-temperature applications due to their oxidation stability.^[2] Although their figure of merit is lower compared to other material systems like tellurides or half-Heusler compounds,^[3] thermoelectric oxides have application potential for energy harvesting because of their viable power factors at high temperatures.^[4] Powering of a mobile phone by an oxide


thermoelectric generator has been successfully demonstrated by Funahashi et al. in 2006.^[5] In several review articles, calcium cobaltite ($\text{Ca}_3\text{Co}_4\text{O}_9$, CCO) and calcium manganate (CaMnO_3 , CMO) are considered to be very promising material systems for application in high-temperature thermoelectric generators.^[2,6,7] The use of ceramic multilayer technology, well established for cost-effective large-scale production of multilayered ceramic capacitors^[8] and circuit boards in low-temperature co-fired ceramics technology,^[9] is an attractive route for the production of cheap multilayered thermoelectric generators (MLTEG) for low power applications. This approach was exemplarily demonstrated using $\text{Ni}_{0.9}\text{Mo}_{0.1}$ as p-type thermoelectric, $\text{La}_{0.035}\text{Sr}_{0.965}\text{TiO}_3$ as n-type thermoelectric, and $\text{Y}_{0.03}\text{Zr}_{0.97}\text{O}_2$ as insulator.^[10] Slightly modified concepts such as the transverse MLTEG, where the stack plane is tilted to the temperature gradient, were even produced with CCO or CMO, respectively.^[11,12] An MLTEG in which

CCO and CMO are combined has not yet been presented. In general, the fabrication of such a module requires the adjustment of the sintering intervals and thermal expansion of the ceramics involved, the selection of a suitable metallization, and an understanding of the interfacial reactions between the different layers. Matched thermal expansion coefficients are important to minimize internal stresses during cooling of the module after sintering and during operation at higher temperatures. In case of CCO/CMO, the thermal expansion coefficients are sufficiently similar, but the sintering temperature of CMO must be lowered, which is investigated in detail in another study.^[13] A glass-ceramic composite suitable as insulation layer between CCO and CMO has also been reported.^[14]

Building on this work, it is now logical to manufacture a multilayer component from this material system and thereby test the feasibility of the multilayer approach experimentally. This was carried out in the present study. The experimental prototype was not thermoelectrically functional due to excessive internal electrical resistance. Analysis of the microstructure revealed vertical cracks in the CMO layers and the formation of different reaction layers at the various interfaces. This raises the question if the failure of the CMO is related to the formation of the reaction layers.

Assuming that the thermal expansion of CCO and CMO is sufficiently similar to allow co-firing,^[13] it can be hypothesized

P. Stargardt, S. Bresch, R. Falkenberg, B. Mieller
Department 5 – Materials Engineering
Bundesanstalt für Materialforschung und -prüfung (BAM)
Unter den Eichen 87, 12205 Berlin, Germany
E-mail: bjoern.mieller@bam.de

 The ORCID identification number(s) for the author(s) of this article can be found under <https://doi.org/10.1002/pssa.202300956>.

© 2024 The Authors. physica status solidi (a) applications and materials science published by Wiley-VCH GmbH. This is an open access article under the terms of the Creative Commons Attribution License, which permits use, distribution and reproduction in any medium, provided the original work is properly cited.

DOI: 10.1002/pssa.202300956

that failure-relevant residual stresses are generated by the reaction layers. To test this hypothesis, the thermal and mechanical properties of the reaction layers were determined and the residual stresses in the multilayer were calculated numerically. This allows a comparison of the stress distribution in a hypothetical multilayer without reaction layers with the stress distribution in the real component to assess the impact of the reaction layers.

The presented study covers the manufacturing of the multilayer prototype from powder to component, the identification of the reaction layers by energy-dispersive X-ray spectroscopy (EDX) and X-ray diffraction (XRD) analyses, a compilation of thermal and elastic properties from literature and specially prepared samples, and the numerical calculation of stress distributions. It is complemented by data on the biaxial strengths of the main constituents CCO and CMO to discuss the damage potential of the calculated internal stresses.

2. Results

2.1. Multilayer Characterization

The multilayer prototype is macroscopically intact. Scanning electron micrographs of a polished cross section of the inner part are shown in **Figure 1**. Metallization is not shown in this image section. The individual layers can be clearly distinguished by their gray value and thickness (Figure 1a). The EDX mapping shows a clear separation of the different layers (Figure 1b). No warping or other deformations are observed. The thicknesses of the different layers are CCO $160 \pm 6 \mu\text{m}$, CMO $100 \pm 6 \mu\text{m}$, insulation $12 \pm 5 \mu\text{m}$, and metallization $6 \pm 1 \mu\text{m}$. The screen-printed insulation layers, identified by the Si signal in Figure 1b, show significant variations in layer thickness. This indicates process fluctuations during screen printing in the production of the prototype. A horizontal crack in the central insulation layer is visible in the secondary electron (SE) contrast (Figure 1a). As the other insulation layers are crack free, the one crack may be an artifact of preparation or a consequence of errors in the screen-printing process. It can be assumed that under stable production conditions it is possible to manufacture the insulating layers without defects. In the CMO layers, which can be clearly identified by the Mn signal, many vertical cracks can be recognized by means of in-lens contrast (Figure 1c). Some of these vertical cracks continue in the insulation layers and even in the CCO layers.

A closer examination of the interfaces in **Figure 2** allows the identification of reaction layers at the different interfaces.

Figure 2a provides a schematic overview of the layer sequence and the location of the detailed interface images shown in Figure 2b–e. The interface between CMO and insulation is shown in Figure 2b. The upper image area shows the CMO layer. In the transition to the insulation (downward in the image), a Ca-depleted layer occurs (designated “1”). Further down, already in the insulation, a Ca-rich and Ba-depleted region is visible (designated “2”). **Table 1** summarizes the element concentrations in the respective layers. Based on these, reaction layer “1” could be CaMn_2O_4 (marokite). Accordingly, layer “2” could be calcium silicate, CaSiO_3 . Isolated Ba signals are visible in the CMO layer. These are probably artifacts from sample preparation.

The interface between insulation and CCO is shown in Figure 2c, with CCO in the lower half of the picture. The SE contrast on the right side of the image shows a crack in black. Above the crack, a Ca-rich layer is identified (designated “3”). A noticeable light gray layer below the crack contains only Co and O (designated “4”). Considering the element concentrations (Table 1), these could be calcium oxide (CaO) and cobalt oxide (Co_3O_4), respectively.

At the top and bottom of the multilayer, the CCO is in contact with the alumina release tape. Figure 2d shows this interface with alumina in the upper half of the picture. A calcium and oxygen-rich layer can be identified on the alumina side of the interface (designated “5”). According to the concentrations (Table 1), this could be a monocalcium aluminate layer (CaAl_2O_4). In the CCO below, a thin-layer enriched in Co and O is found (designated “6”). According to the concentrations, this could be another Co_3O_4 layer.

Figure 2e shows a section in which the CCO, CMO, and insulation are in contact with the Ag metallization. CMO is found in the upper half of the image, CCO in the bottom half. The insulation in between, recognizable by the Al and Ba signals, is on the left-hand side. The Ag metallization is visible in the right third of the image. Apart from the reaction layers already described, no further reaction layers with Ag are discernible.

The thicknesses of all identified reaction layers are 1–3 μm (see Table 1). Two reaction layers were found at each interface. Compared to the thickness of the main layers, the reaction layer affected zone is roughly 1.8% of CCO, 3% of CMO, and 10% of the insulation, respectively.

Due to the low thickness of the reaction layers, the porosities of these layers are difficult to measure. CaSiO_3 (layer 2), CaO (layer 3), and Co_3O_4 (layer 4) seem rather dense. CaMn_2O_4 (layer 1) and CA (layer 5) are rather porous with porosity levels in the range of the CMO and alumina release tape, respectively.

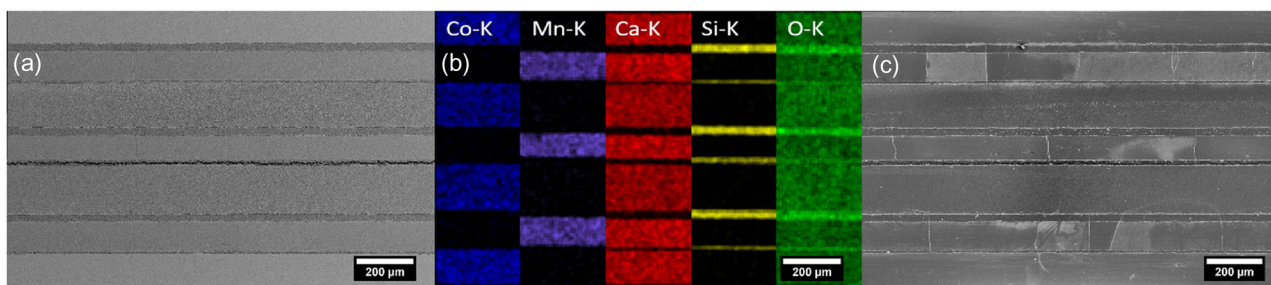


Figure 1. Polished cross section of the sintered multilayer: a) SE detector, b) element distribution (EDX), and c) in-lens detector.

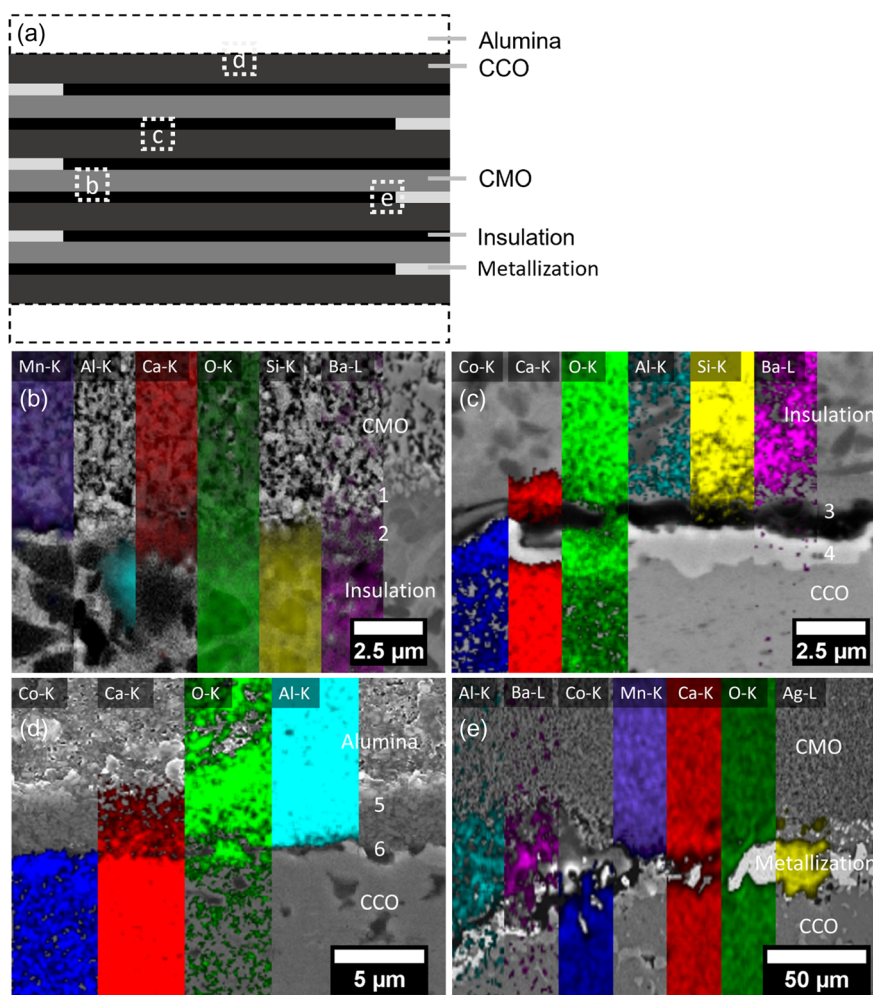


Figure 2. a) Element distributions across interfaces in the sintered multilayer; b–e) schematic structure of the multilayer with localization of the different element mappings.

Table 1. Element concentration in the reaction layers and calculated phases.

Reaction layers in between	Number	Element concentration [mol%]	Calculated phase	Layer thickness [μm]
CMO and insulation	1	Ca–Mn–O 12–25–63	CaMn ₂ O ₄	3
	2	Ca–Si–O 16–22–62	CaSiO ₃	1
CCO and insulation	3	Ca–O 33–67	CaO	1
	4	Co–O 55–44	Co ₃ O ₄	3
CCO and alumina release tape	5	Ca–Al–O 16–31–52	CaAl ₂ O ₄	2
	6	Co–O 59–41	Co ₃ O ₄	1

For phase calculation of the reaction layers, the quantitative element concentrations obtained by EDX were used. The results of the calculations needed to be verified due to the intrinsic uncertainties of the EDX method. Therefore, the grazing incident XRD was performed at the surface of the multilayer sample where CCO and alumina release tape formed an interface during sintering (reaction layer 5 and layer 6 in Figure 2).

Figure 3a,b shows the measured XRD spectra. For reaction layer 6 apart from CCO, cobalt oxide (Co₃O₄) was identified as additional phase (see Figure 3a). The reaction layer 5 is mainly composed of CA as shown in Figure 3b. The grazing incident XRD patterns confirm the previously calculated phases for the reaction layers at the interface of the CCO and the alumina release tape. Based on the good agreement between XRD and calculated phases at the surface of the multilayer, it can be estimated that the EDX analysis is sufficiently accurate to analyze the chemical composition of the inner reaction layers.

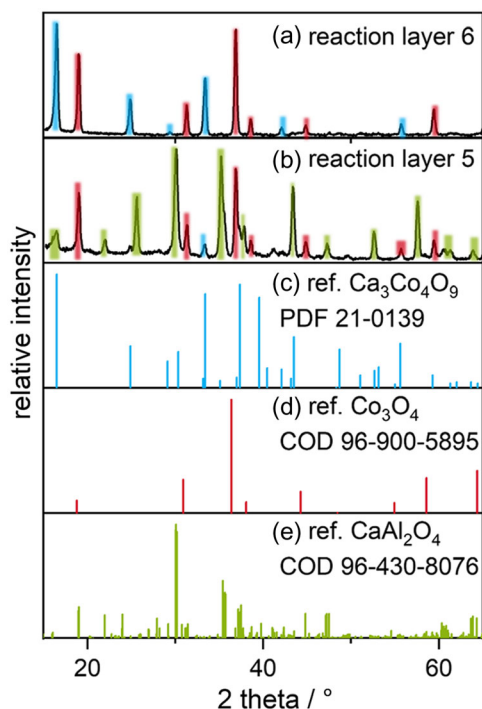


Figure 3. Surface analysis by grazing incident XRD of a) reaction layer 6 and b) reaction layer 5; c–e) reference patterns.

In the following, a dataset of thermal and elastic properties of the identified layers is provided. Therefore, the materials were synthesized, their phase composition and phase purity were

analyzed, and the thermal expansion and elastic properties were measured. These measurements were supplemented by literature data.

The phase composition and phase purity of the prepared powders were analyzed by powder XRD. **Figure 4a** shows the XRD pattern and Rietveld analysis of the calcined CMO powder. The powder consists of CMO and CuO, no secondary phase is detected. According to the quantitative Rietveld analysis, the powder contained 97 wt% CaMnO_3 and 3 wt% CuO (Bragg R factor = 4.6, reduced $X^2 = 7.9$). The Rietveld analysis differs slightly from the 4 wt% CuO added during milling. **Figure 4e** shows the XRD pattern of the calcined CA powder. The main peaks can be allocated to the desired CaAl_2O_4 phase. Three peaks at 2θ angles of 18° , 33.5° , and 40° can be assigned to a minor secondary impurity phase: $\text{Ca}_{12}\text{Al}_{14}\text{O}_{33}$. Quantitative analysis by Rietveld method resulted in 96 wt% CaAl_2O_4 and 4 wt% $\text{Ca}_{12}\text{Al}_{14}\text{O}_{33}$ as secondary phase (Bragg R factor = 4.2, reduced $X^2 = 4.0$). This is considered as sufficiently pure to analyze the coefficient of thermal expansion. The prepared CCO powder is phase pure according to XRD analysis published in our previous work.^[15] The sintered insulation material is composed of 13 wt% celsian, 36 wt% quartz, and 51 wt% residual glass according to quantitative Rietveld method, as published before.^[14]

Sintered CMO and CCO samples have relative densities of 70% and 90%, respectively. The CaAl_2O_4 sample has a relative density of 75% and the insulation sample has a relative density of 96%. It should be noted that CaAl_2O_4 , CMO, and insulation were conventionally sintered, whereas the multilayer sample was pressure-assisted sintered with 7.5 MPa. However, the density values are in good accordance with literature data for pressure-assisted sintered samples from the same materials.^[13–15]

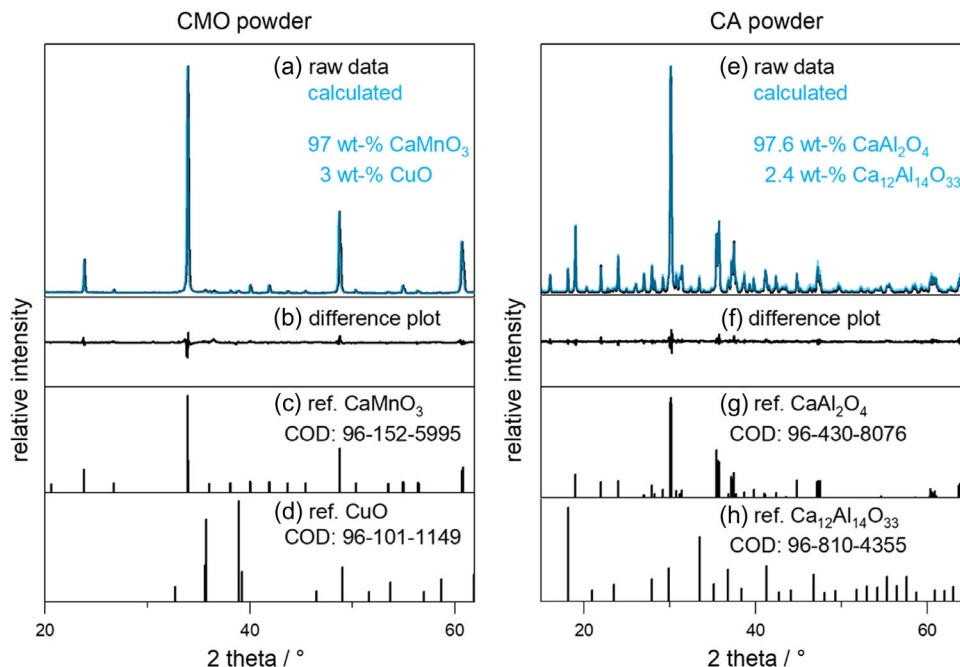


Figure 4. Powder XRDs and Rietveld analysis of synthesized a) CMO powder and e) CA powder with raw data in black and calculated pattern in blue. b,f) The difference plots between calculated and raw data are shown, respectively. c,d,g,h) The used respective reference data.

Table 2. Linear coefficient of thermal expansion of layer materials and reaction layers.

Material	$\alpha_{20-600\text{ }^\circ\text{C}}$ in $10^{-6} [\text{K}^{-1}]$	Source
CCO	10.79	This study
CaAl ₂ O ₄	6.76	This study
Insulation	13.3	This study
CMO	12.75	This study
Co ₃ O ₄	10.43	[26]
CaO	13.1	[27]
CaSiO ₃	21	[28]
CMO composite (CMO + CaMn ₂ O ₄)	19.7	[16]

2.2. Thermal Expansions and Elastic Properties of Single Materials

Table 2 summarizes the coefficients of thermal expansion of all materials. A temperature regime from 20 to 600 °C was evaluated with respect to the glass-transition temperature of the insulation at 600 °C.^[14] Further values were compiled from literature. Please note that the thermal expansion data of a composite material from CMO and CaMn₂O₄ instead of pure CaMn₂O₄ is used.^[16]

Figure 5a shows a Weibull plot of the biaxial strength of CCO and CMO. The characteristic strength, at which 63% of the samples failed, amounts to 227 MPa for CCO and 68 MPa for CMO, respectively. Weibull moduli of 6 and 13 were determined for CCO and CMO, respectively.

Table 3 shows the results of the Young's modulus, shear modulus, and the Poisson ratio at room temperature for all identified reaction layers and layer materials. The results of the high-temperature measurement are depicted in **Figure 5b**. The Young's modulus of CMO is decreasing with rising temperature as expected from literature.^[17] The glass-ceramic insulation shows this behavior to a much lesser extent. Due to the glass-transition region of the glass phase, the measurement was stopped at 600 °C.^[14] Elastic constants depend on the microstructure, especially on porosity.^[18] The literature data of CCO, Co₃O₄, CaO, and CaSiO₃ have a similar porosity as the respective layers

Table 3. Elastic constants of layer materials and reaction layers at room temperature.

Material	Young's modulus [GPa]	Shear modulus [GPa]	Poisson ratio	Porosity [%]	Source
CMO	81	32.7	0.24	30	This study
insulation	80	32.5	0.26	4	This study
CCO	52	20.8	0.25	10	Ref. [29], hot pressed with 5 MPa
CaAl ₂ O ₄	107	43	0.25	0	[30]
Co ₃ O ₄	218	87	0.25	1	[31]
CaO	202	74	0.21	0	[30]
CaSiO ₃	73	29.6	0.235	1	[32]

in the multilayer sample. Only for CaAl₂O₄ the elastic properties should be adapted to the porosity of the layer which is approximately 30%. The porosity dependency of the Young's modulus can be estimated according to $E = E_0 \cdot e^{-4P}$ with Young's modulus of sample with 0% porosity E_0 , and porosity P .^[18] For 30% porous CaAl₂O₄, this gives $E = 32$ GPa and similarly 13 GPa for the shear modulus.

2.3. Numerical Calculation of Internal Stresses

The stress distribution plot in **Figure 6a** shows that the stress distribution in the multilayer is homogeneous and independent of length, apart from short range disturbance at the edge. Thus, the reduction of length in the model is admissible. Normal stress in x direction exported along the path through the middle of the domain presented in **Figure 6a** is shown in **Figure 6b**. Evaluating the middle of the domain guarantees that the results are free of edge disturbances confined within a short distance from the left and right (not shown) boundaries. The blue line shows the stress values for the multilayer without reaction layers. The multilayer with reaction layers is represented by the red line. Comparing both cases, it stands out that a) the reaction layers show high internal stresses due to their significantly different material properties and b) the stresses in the principal layers CMO and CCO

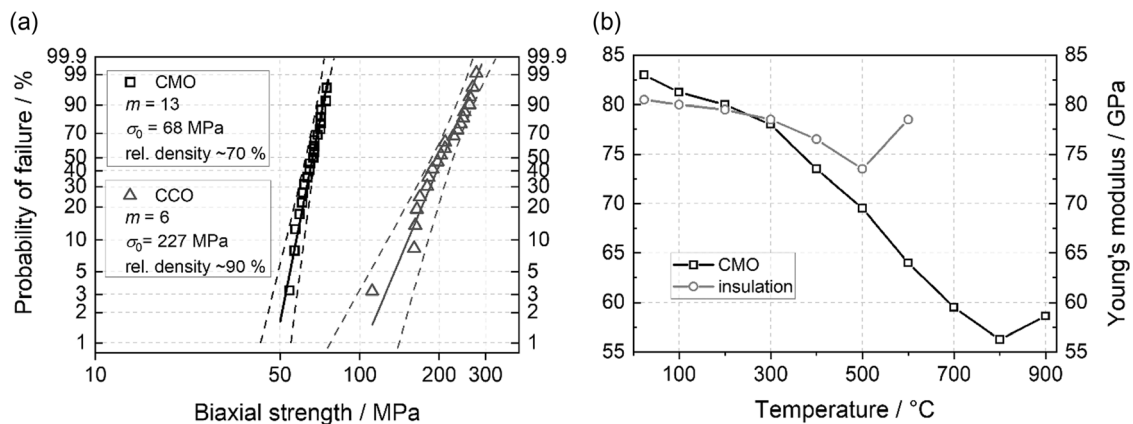


Figure 5. a) Weibull plot of thermoelectric oxides strength results and b) high-temperature Young's modulus results of CMO and insulation.

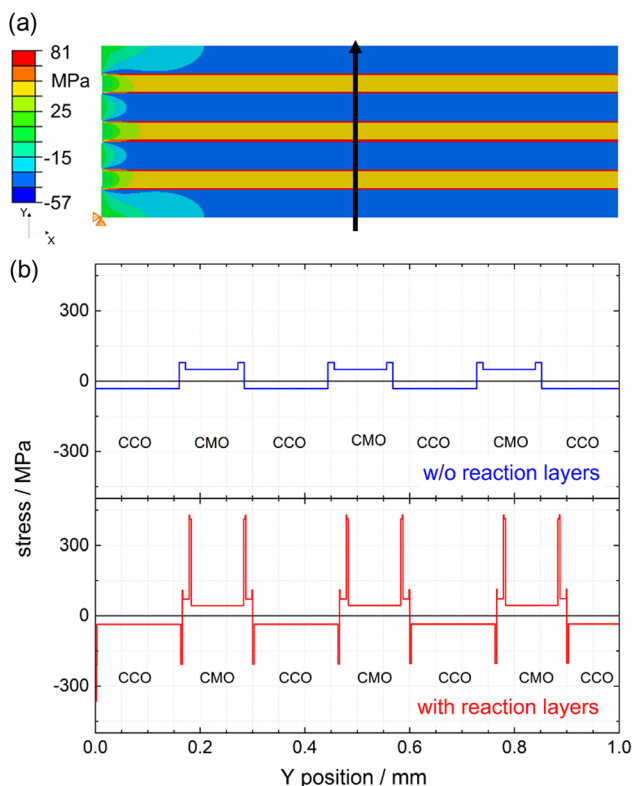


Figure 6. Distribution of internal stresses in the multilayers calculated by FEM with and without consideration of reaction layers in terms of orthogonal normal stress in x direction: a) left half of the contour plot of multilayer without reaction layers including path for stress evaluation, and b) normal stress in x direction along evaluation path; positive values correspond to tensile stress.

are only slightly affected by the presence of the reaction layers. The stresses are evaluated to approximately $-32/-37$ MPa for CCO and $50/43$ MPa for CMO without/with reaction layers, respectively. This means that both in the simplified model without reaction layers and in the realistic model with reaction layers, the CMO layers are under tensile residual stress and the CCO layers under compressive residual stress.

3. Discussion

Fabrication of a multilayer prototype from CCO, CMO, insulation, and metallization lead to a macroscopically intact but microscopically cracked component. Many vertical cracks were detected in the CMO layers. Analyses of the co-fired multilayer resulted in the identification of five different reaction layers at the different interfaces. The properties of the reaction layers differ significantly from CMO and CCO. However, there is only a subtle effect on the distribution of internal stresses in the prototype multilayer. Compared to a virtual multilayer without reaction layers, the presence of reaction layers even reduces the internal tensile stress in CMO by 14%. To evaluate the risk of failure, the internal stress has to be compared to the strength of the material. The data on the biaxial flexural strength of

CMO shown in Figure 5 indicate a characteristic strength of 68 MPa and no failure at stress up to 50 MPa. In the multilayer, however, in-plane tensile stress is effective on the CMO layer. It can be assumed that in-plane tensile stresses lead to failure at lower stress levels compared to flexural stresses. In PZT ceramics for example, in several studies, bending strength corresponds to nearly twice the tensile strength.^[19] According to Leguillon et al. a ratio between flexural strength and tensile strength can be calculated depending on the Weibull modulus m .^[20] As the relation is not derived for biaxial strength testing, alternatively pure bending (Equation (1)) and three-point bending (Equation (2)) are considered here, respectively.

$$R_{PB} = [2(m + 1)]^{(1/m)} \quad (1)$$

$$R_{3P-B} = [2(m + 1)^2]^{(1/m)} \quad (2)$$

With $m = 13$ for CMO, a bending to tensile strength ratio of $R_{PB} = 1.3$ or $R_{3P-B} = 1.6$ is calculated accordingly. The strength under tensile load is therefore lower than under bending. It is therefore likely that, under tensile load, a relevant probability of failure in the CMO layers already exists at stresses of less than 50 MPa.

It should be noted that the biaxial strength testing was performed on dry-pressed specimen. Although sintered density has been adjusted, microstructure and defect population may be somewhat different in the CMO layers of the multilayer.

As the presented FE model contains simplifications and idealizations, local stress concentrations exceeding the determined peak values of $50/43$ MPa are not explicitly taken into account but must be expected. Those simplifications are, e.g., the assumption of ideal straight edges between layers and the neglect of any flaws, such as precipitations, defects, or pores. As presented in Figure 2, boundaries between layers show an uneven topography and even inhomogeneities in the material. Both are reasonable causes for local stress concentrations. Furthermore, homogeneous material properties for each layer are assumed, which idealizes an expected gradient distribution due to the sintering process. This procedure cannot account for elevated stress values due to locally varying material properties. Moreover, as this simulation only compares two temperature states and does not incorporate transient heat conduction, any effects due to temperature gradients cannot be calculated. Taking these discrepancies into account, the actual residual tensile stresses in the CMO layers of the prototype are likely to be higher than the calculated 43 MPa.

In summary, it is concluded that the tensile strength of the CMO is probably lower than 50 MPa and the residual tensile stresses are probably higher than 43 MPa. It is therefore reasonable to assume that the cracks in the CMO are a result of the residual tensile stresses. Contrary to the hypothesis, the critical residual stresses are not caused by the formation of the reaction layers. This study rather shows that although CMO and CCO principally appear to be suitable for co-firing, internal stresses arise in specific multilayer designs that are high enough to cause cracking. From a purely mechanical point of view, these stresses could be altered by specifically changing the CMO and CCO layer thickness. With regard to the desired application as a thermoelectric generator, however, electrical design aspects should also be

taken into account. Most importantly, the ratio of the cross area of the thermoelectric materials (A_p and A_n) should be equal to the square root of the reciprocal ratio of their electric conductivities (σ_p and σ_n , see Equation (3)) to minimize the electrical resistance of the generator.^[21]

$$\frac{A_p}{A_n} = \sqrt{\frac{\sigma_n}{\sigma_p}} \quad (3)$$

Consequently, when designing an MLTEG consisting of CCO and CMO, mechanical and electrical aspects must be considered together to facilitate a successful co-firing. This was beyond the scope of the present study. Still, the data reported here may serve as starting point for such a development. Furthermore, the poor densification of the CMO layer in the prototype multilayer leaves room for improvement, for example, by an increased pressure during co-firing or other means. This could increase the strength and thus the tolerable residual stress.

4. Conclusion

A multilayer module consisting of the thermoelectric oxides CCO and CMO, including insulation layers and AgPd metallization, was fabricated by tape casting, screen printing, stacking, and pressure-assisted sintering with 7.5 MPa at 900 °C. Vertical cracks were found in the CMO layers and identified as the cause of the high internal resistance of the multilayer, which prevents thermoelectric characterization. Five different reaction layers were identified and characterized in terms of composition, thermal, and mechanical properties. The residual stresses in the multilayer after cooling were assessed by numerical calculations. The experimental results show that the reaction layers exhibit significantly different thermal expansion and mechanical properties compared to the principal layers CCO and CMO. However, the numerical calculations show that the presence of the reaction layers has only a minor influence on the residual stresses in the principal layers. Regardless of the reaction layers, co-firing leads to tensile stresses in the CMO layers at the level of the biaxial strength. Regarding the manufacturability of such a multilayer, the reaction layers appear to be tolerable. The main issue is the insufficient strength of the CMO. For successful co-firing, either the thickness of the layers would have to be adjusted for better stress distribution or the strength of the CMO layer would have to be increased through better densification during sintering. The data provided here can be helpful for the future design of thermoelectric multilayer generators in the CCO/CMO material system to take mechanical aspects into account in addition to electrical criteria.

5. Experimental Section

Powder Production and Multilayer Fabrication: Thermoelectric oxides were synthesized using classical mixed oxide route. Stoichiometric amounts of CaCO_3 (99%, low-alkali, Riedel-de Haën) and Co_3O_4 (99.97%, Chem-PUR) or CaCO_3 (99%, low-alkali, Riedel-de Haën), MnCO_3 ($\geq 99.9\%$, Aldrich Chemistry), and $\text{Sm}(\text{OH})_3$ (Carl Roth GmbH + Co., KG) were attrition milled (ZrO_2 -grinding media, 45 min, 800 s^{-1} , moliNEX, Netzsch) and then calcined at 900 °C for 12 h or at 1250 °C for 2 h to form $\text{Ca}_3\text{Co}_4\text{O}_9$ (CCO) or $\text{Ca}_{0.98}\text{Sm}_{0.02}\text{MnO}_3$ (CMO),

respectively. The calcined mixtures were then crushed with a planetary ball mill (agate grinding balls, 20 min, 215 min^{-1} , Pulverisette 5, Fritsch) and fine milled using an attrition mill (ZrO_2 -grinding media, 800 s^{-1} , moliNEX, Netzsch) for 45 min (CCO) or 4 h (CMO). And, 4 wt% CuO were added to CMO as sintering additive during the attrition milling.^[13] The resulting mean grain size was 4 μm (laser diffraction method) for CCO and 0.1 μm (volume specific surface area, mean particle diameter derived from true density and specific surface) for CMO. Tape-casting slurries were produced by mixing the thermoelectric oxides with polyvinyl butyral (Sekisui Specialty Chemicals Europe S.L.), dibutyl phthalate (Laborchemie Apolda GmbH), Rhodafac RE-610 (SOLVAY GmbH), and a solvent mixture containing ethanol (Merck KGaA), methyl ketone (Merck KGaA), and cyclohexanone (Merck KGaA) for 24 h in porcelain containers on a rolling bench. The slurries were tape cast on a tape-casting machine (doctor blade method, Netzsch). The resulting tapes (width = 150 mm) had a thickness of 150 μm (CCO) or 85 μm (CMO), respectively. For the insulation material, 55 vol% of the glass G69250 (Heraeus) and 45 vol% of quartz (SIKRON SF 600, Quarzwerke) were attrition milled for 1 h (moliNEX, Netzsch). A commercial screen-printing medium (801 026, Ferro) was added to the powder and homogenized in a planetary ball mill (60 min, Pulverisette 5, Fritsch) to produce a screen-printable paste. On the thermoelectric tapes, layers of the insulation paste and stripes of the metallization paste AgPd (DP6146, Dupont) were screen printed (P-200A, Keko Equipment). The printed tapes of CCO and CMO were alternately stacked and laminated (custom-made heated stacking tool, 70 °C, 20 MPa, 20 min), sandwiched in between two alumina release tapes (Ceramtape A, CeramTec GmbH) and laminated again. The laminate was sintered in a commercial low temperature co-fired ceramic sintering press (900 °C, 7.5 MPa, PHP-630, ATV Technologie GmbH). After sintering, the release tapes were carefully removed by scrubbing. The produced multilayer stack comprising three thermoelectric pairs of CCO and CMO had a thickness of 1 mm, a length of 20 mm, and a width of 20 mm.

Characterization of the Sintered Multilayer: The sintered multilayer was analyzed by scanning electron microscopy (SEM, Gemini Supra 40, ZEISS) on polished samples. Secondary electron detector and in-lens detector were used for different contrasts. The element distributions and concentrations were determined by EDX (NSS 3.1, Thermo) at $U_A = 15$ kV on at least five different points on the sample. Off-color images were taken for better visualization of the element distribution. Furthermore, the multilayer was phase-analyzed at the surface by grazing incident XRD (3000 TT, Seifert) with Cu-K α light source (1.5418740 Å). The patterns were evaluated with the software package Match! 3.

The elemental concentration data obtained by EDX was used to calculate possible phases formed during sintering. The average was used for calculation, and the measured element mass ratio was converted to an atomic ratio x using Equation (4).

$$x_i = \frac{w_i/M_i}{\sum_{k=1}^n (w_k/M_k)} \quad (4)$$

w is the mass ratio of the specific element and M is the molar mass of that element. By dividing the atomic ratios by the smallest ratio in the respective composition, the composition of the corresponding phase was calculated.

Preparation of Single Materials: Samples of the single materials and the main reaction layer phase were prepared for mechanical analysis. The glass-ceramic insulation, CMO, and the identified reaction layer phase CaAl_2O_4 (CA) were synthesized. Powders of the insulation and the CMO were prepared as described earlier. For the CA, stoichiometric amounts of CaCO_3 (99%, low-alkali, Riedel-de Haën) and $\gamma\text{-Al}_2\text{O}_3$ (Merck) were attrition milled (ZrO_2 -grinding media $d = 2\text{--}3$ mm, 45 min, 800 s^{-1} , moliNEX, Netzsch) and calcined at 1400 °C to form CA. The calcined mixtures were then crushed with a planetary ball mill (agate-grinding balls, 20 min, 215 min^{-1} , Pulverisette 5, Fritsch) and fine milled using an attrition mill (ZrO_2 -grinding media $d = 2\text{--}3$ mm, 45 min, 800 s^{-1} , moliNEX, Netzsch). After milling, the calcined powders were characterized by powder XRD (Ultima IV, Rigaku) with Cu-K α radiation

(1.5418740 Å) to confirm the phase compositions. The patterns were analyzed with the software package Match! 3.

For sample preparation, the calcined powders (CMO, insulation, and CA) were mixed with 1.5 wt% pressing agents (Zusoplast 9002 and OptapixAC95, Zschimmer & Schwarz). The following samples were uniaxially pressed with 60 MPa (KV247.02, Rucks Maschinenbau): bars for stiffness measurement (120 × 8 × 5 mm), bars for thermal expansion measurement (25 × 5 × 5 mm), and disc samples for strength testing ($d = 12$ mm, $h = 3$ mm). The samples were sintered in air at 900 °C (insulation, L16/14, Nabertherm), 955 °C (CMO, L16/14, Nabertherm), or 1370 °C (CA, FHT180, Ceram-Aix). The sinter profiles were adapted to match the density of the respective layer in the multilayer sample.

CCO samples were prepared by multilayer technology because pressure-assisted sintering was necessary for sufficient densification. Green tapes of CCO were stacked to 1 mm thickness. Lamination and sintering were performed as previously described. Bar (75 × 8 × 0.5 mm) and disk specimens ($d = 10$ mm) were prepared by cutting.

The linear thermal expansion was measured on specimens with plane-parallel ends (length: 25 mm, width: 4 mm) with a heating rate of 5 K min⁻¹ in air. A push-rod dilatometer (DIL402c, Netzsch) with a contact force of 0.25 N was used. The coefficient of thermal expansion was calculated according to Equation (5).

$$\alpha(T_R; T) = \frac{l(T) - l_0}{l_0} \frac{1}{T - T_R} \quad (5)$$

with the thermal expansion coefficient α in K⁻¹; the length at room temperature, l_0 ; the temperature-dependent length, $l(T)$; the room temperature, T_R ; and the upper temperature, T .

Biaxial strength was determined by ball on three ball tests on 21 disk samples ($d = 10$ mm) of CMO and CCO (7 mm ball diameter, Z5, Zwick/Roell), respectively. A detailed description of the ball on three ball method can be found in literature.^[22] The results were evaluated by Weibull plots using maximum likelihood method to fit the data. Room-temperature elastic constants of all materials involved were determined by vibrational method. The elastic constants of CMO and insulation as a function of temperature were determined by sonic resonance measurement on 70 × 6 × 2 mm bars from room temperature to 900 and 600 °C, respectively. This method was first described by Förster^[23] and was performed according to ASTM E1875-20a.^[24]

Bulk density (ρ) of the sintered samples was determined by Archimedes method (according to standard DIN EN 623-2) according to Equation (6).

$$\rho \approx \frac{M_1 \cdot \rho_w}{M_3 - M_2} \quad (6)$$

with the dry sample mass, M_1 ; the submerged sample mass, M_2 ; the water-soaked sample mass, M_3 ; and the density of water, ρ_w .

Numerical Calculation of Internal Stresses: The cooling of the multilayer compound from 600 to 100 °C was numerically simulated by means of the finite-element method (FEM) to assess the developing in-plane stresses in the different layers. Two domain configurations were simulated and compared to study the relevance of the reaction layers for the stress response of the principal layers CCO and CMO: 1) without reaction layers; and 2) with reaction layers. The domains were discretized using second-order plane-strain triangle elements. A statically determinate system was defined using boundary conditions that restricted displacements at the bottom left corner in x and y directions and at the bottom right corner in y direction. Therefore, evolving thermal stresses were not caused by the boundary conditions itself but by the strains induced by inhomogeneously distributed internal properties of the domain layers. Since only the stresses at 600 and 100 °C were of interest and transient stresses over the entire temperature range were not relevant, a fully coupled temperature-displacement analysis was not necessary. The mechanical equilibrium together with linear-elastic isotropic material behavior at 100 °C was evaluated using an initial condition of $T = 600$ °C. The length of the domain was reduced to 5 mm to minimize computational effort without altering the results. The input deck for the calculation job is publicly available.^[25]

Acknowledgements

The authors like to thank Prof. Dr. Raúl Bermejo and Roman Papšik (Chair of Structural and Functional Ceramics, Montanuniversität Leoben) for discussions of internal stress calculations. The support of the BAM employees Sigrid Benemann (SEM imaging), Mario Sahre (XRD measurements), Faruk Bayram (CTE measurements), and Sven Ruster (machining for sample preparation) is also gratefully acknowledged.

Open Access funding enabled and organized by Projekt DEAL.

Conflict of Interest

The authors declare no conflict of interest.

Data Availability Statement

The data that support the findings of this study are openly available in Zenodo at <https://doi.org/10.5281/zenodo.10351846>, reference number 10351846.

Keywords

ceramic multilayers, co-firings, internal stresses

Received: December 19, 2023

Revised: April 8, 2024

Published online:

- [1] N. Jaziri, A. Boughamoura, J. Müller, B. Mezghani, F. Tounsi, M. Ismail, *Energy Rep.* **2020**, *6*, 264.
- [2] K. Koumoto, R. Funahashi, E. Guilmeau, Y. Miyazaki, A. Weidenkaff, Y. Wang, C. Wan, X. Zhou, *J. Am. Ceram. Soc.* **2013**, *96*, 1.
- [3] J. Wei, L. Yang, Z. Ma, P. Song, M. Zhang, J. Ma, F. Yang, X. Wang, *J. Mater. Sci.* **2020**, *55*, 12642.
- [4] D. Narducci, *Appl. Phys. Lett.* **2011**, *99*, 102104.
- [5] R. Funahashi, M. Mikami, T. Mihara, S. Urata, N. Ando, *J. Appl. Phys.* **2006**, *99*, 066117.
- [6] J. W. Fergus, *J. Eur. Ceram. Soc.* **2012**, *32*, 525.
- [7] J. He, Y. Liu, R. Funahashi, *J. Mater. Res.* **2011**, *26*, 1762.
- [8] K. Hong, T. H. Lee, J. M. Suh, S.-H. Yoon, H. W. Jang, *J. Mater. Chem. C* **2019**, *7*, 9782.
- [9] Y. Imanaka, *Multilayered Low Temperature Cofired Ceramics (LTCC) Technology* Springer-Verlag, New York, NY **2005**.
- [10] S. Funahashi, T. Nakamura, K. Kageyama, H. Ieki, *J. Appl. Phys.* **2011**, *109*, 124509.
- [11] A. Bochmann, T. Reimann, T. Schulz, S. Teichert, J. Töpfer, *J. Eur. Ceram. Soc.* **2019**, *39*, 2923.
- [12] T. Reimann, A. Bochmann, A. Vogel, B. Capraro, S. Teichert, J. Töpfer, *J. Am. Ceram. Soc.* **2017**, *100*, 5700.
- [13] S. Bresch, B. Mieller, R. Moos, T. Rabe, *AIP Adv.* **2022**, *12*, 085116.
- [14] S. Bresch, B. Mieller, P. Mrkwitschka, R. Moos, T. Rabe, *J. Am. Ceram. Soc.* **2022**, *105*, 2140.
- [15] S. Bresch, B. Mieller, D. Schönauer-Kamin, R. Moos, T. Reimann, F. Giovannelli, T. Rabe, *J. Am. Ceram. Soc.* **2021**, *104*, 917.
- [16] N. Kanas, M. Bittner, T. D. Desissa, S. P. Singh, T. Norby, A. Feldhoff, T. Grande, K. Wiik, M.-A. Einarsrud, *ACS Omega* **2018**, *3*, 9899.
- [17] J. B. Wachtman, W. E. Tefft, D. G. Lam, C. S. Apstein, *Phys. Rev.* **1961**, *122*, 1754.
- [18] C. B. Carter, M. G. Norton, *Ceramic Materials - Science and Engineering*, Springer-Verlag, New York, NY **2007**.

- [19] T. Fett, D. Munz, G. Thun, *J. Mater. Sci. Lett.* **1999**, *18*, 1899.
- [20] D. Leguillon, E. Martin, M.-C. Lafarie-Frenot, *C. R. Mec.* **2015**, *343*, 275.
- [21] *CRC Handbook of Thermoelectrics*, 1st ed., (Ed: D.M. Rowe), CRC Press, Boca Raton, FL **1995**.
- [22] A. Börger, P. Supancic, R. Danzer, *J. Eur. Ceram. Soc.* **2002**, *22*, 1425.
- [23] F. Förster, *Z. Metallkd.* **1937**, *29*, 109.
- [24] ASTM E1875-20a, *Standard Test Method for Dynamic Young's Modulus, Shear Modulus, and Poisson's Ratio By Sonic Resonance*, ASTM International, West Conshohocken, PA **2020**.
- [25] R. Falkenberg, *BAMresearch/MultilayerInternalStresses: Supplementary Material*, <https://github.com/BAMresearch/MultilayerInternalStresses.git> (accessed: December 2023).
- [26] A. D. D. Broemme, *IEEE Trans. Electr. Insul.* **1991**, *26*, 49.
- [27] A. S. M. Rao, K. Narender, *J. Thermodyn.* **2014**, *2014*, 123478.
- [28] R. J. Hill, I. Jackson, *Phys. Chem. Miner.* **1990**, *17*, 89.
- [29] D. Kenfaui, M. Gomina, D. Chateigner, J. G. Noudem, *Ceram. Int.* **2014**, *40*, 10237.
- [30] M. de Jong, W. Chen, T. Angsten, A. Jain, R. Notestine, A. Gamst, M. Sluiter, C. K. Ande, S. van der Zwaag, J. J. Plata, C. Toher, S. Curtarolo, G. Ceder, K. A. Persson, M. Asta, *Dryad* **2016**, <https://doi.org/10.5061/dryad.h505v>.
- [31] P. Meena, R. Kumar, K. Sreenivas, *Indian J. Pure Appl. Phys.* **2018**, *56*, 890.
- [32] N. I. Demidenko, A. P. Stetsovskii, *Glass Ceram.* **2003**, *60*, 217.